

Impact of coherent scattering on relic neutrinos boosted by cosmic rays

Jiajie Zhang^{1,*}, Alexander Sandrock^{2,†}, Jiajun Liao^{1,‡} and Baobiao Yue^{2§}

¹ School of Physics, Sun Yat-sen University, Guangzhou, 510275, China and

² Faculty of Mathematics and Natural Sciences, University of Wuppertal, 42119 Wuppertal, Germany

Ultra-high-energy cosmic rays (UHECR) scattering off the cosmic relic neutrino background have recently gained renewed interest in the literature. Current data suggest that UHECR are predominantly made of heavy nuclei. Since the energy of relic neutrinos can reach $\sim \mathcal{O}(10)$ MeV in the rest frame of the UHECR, the cross section of heavy nuclei scattering off relic neutrinos can be coherently enhanced, which is similar to the coherent elastic neutrino-nucleus scattering (CE ν NS) observed at low-energy neutrino experiments. We calculate the diffuse flux of relic neutrinos boosted by UHECR by taking into account the contributions from both the coherent and incoherent scatterings. Using current data from the IceCube Neutrino Observatory and the Pierre Auger Observatory, we place constraints on the overdensity of relic neutrinos down to 10^7 . Since the flux of boosted relic neutrinos peaks at an energy of $\sim \mathcal{O}(100)$ PeV, we also entertain the possibility to explain the recently observed KM3NeT event with boosted relic neutrinos from UHECR.

Introduction. The cosmic relic neutrino background (C ν B), a fundamental prediction of the standard cosmological model (Λ CDM), provides a unique probe of the early universe and the evolution of cosmic structure [1–3]. The Λ CDM model predicts that the C ν B today has an average number density of 56 cm^{-3} per spin and flavor degree of freedom with a temperature of 1.95 K [2, 3]. Detecting these relic neutrinos is quite challenging, and requiring experiments with ultra-low energy thresholds. The proposed PTOLEMY experiment [4], which employs the method of capturing relic neutrinos in tritium, is hampered by the Heisenberg uncertainty principle for storing tritium atoms on a graphene sheet [5]. The neutrino number density can be greatly enhanced in a non-standard cosmological history [6], such as those involving dark matter decay into neutrinos [7–9], or new Yukawa interactions of neutrinos [10]. The current strongest experimental constraint is set by the KATRIN experiment, with an upper limit on the local C ν B overdensity $\eta < 9.7 \times 10^{10}$ at the 90% confidence level (CL) [11].

Ultra-high-energy (UHE) cosmic rays (CR) provide a promising avenue for probing C ν B through up-scattering, a concept first introduced by Hara and Sato in the 1980s [12, 13]. Recent studies have used CR scattering on the C ν B to impose constraints on the C ν B overdensity in various contexts. Ref. [14] constrains the overdensity in the ballpark of $\sim 10^{13}$ within the Milky Way and $\sim 10^{11}$ near the blazar TXS 0506+056. A very strong limit of $\sim 10^4$ on the average C ν B overdensity has been placed in Ref. [15]. By considering both elastic scattering (ES) and deep inelastic scattering (DIS), Ref. [16] put a constraint on the weighted overdensities in cosmic-ray reservoirs down to $\sim 10^{10}$. Note that Refs. [14, 15] only consider the proton composition in CR with an oversimplified scattering cross sections, neglecting the significant contribution from heavy nuclei to boost the C ν B.

Current data indicate a dominant heavy-element composition for UHECR, with the proton fraction dropping below 10% for CR energy above 10 EeV [17], which is

also consistent with air shower simulations despite of large uncertainties in hadronic interactions [18]. A pure iron model for UHECR composition is even adopted in some studies [19–21]. In addition, observations from the Pierre Auger Observatory [17], KASCADE-Grande [22], and Telescope Array [23] also show an increasing prevalence of heavy nuclei at the highest energies. Given the significant presence of heavy nuclei in UHECR, the contributions from heavy nuclei in boosting the C ν B cannot be ignored.

For neutrinos with an energy of $\sim \mathcal{O}(10)$ MeV, coherent elastic neutrino-nucleus scattering (CE ν NS) occurs since neutrinos interact with all nucleons in a nucleus collectively, which significantly increase the cross section at low energy neutrino scattering experiments [24]. CE ν NS has been confirmed experimentally by the COHERENT collaboration in 2017 using accelerator-based sources [25]. Subsequent measurements at COHERENT further validated the existence of CE ν NS [26, 27], complemented by observations from the solar [28, 29] and reactor data [30]. In the context of an iron-nuclei UHECR with an energy ~ 10 EeV scattering on a relic neutrino of mass 0.1 eV, the neutrino energy in the nucleus’s rest frame is ~ 20 MeV, which is in the same energy range where CE ν NS is dominant at low energy neutrino scattering experiments. Thus, the coherent enhancement of the cross section for heavy nuclei in CR scattering off the C ν B can be significant.

In this Letter, we study the diffuse flux of the C ν B boosted by the UHECR, taking into account the contributions of heavy nuclei through both the coherent and incoherent scattering channels. Using the data from the IceCube (IC) and the Pierre Auger (PA) Observatory, we place constraints on the C ν B overdensity. The KM3NeT collaboration recently detected a record-breaking neutrino event, KM3-230213A, with an energy of 220_{-110}^{+570} PeV [31]. Interestingly, our prediction of the boosted C ν B by UHECR yield a diffuse flux peaked at $\mathcal{O}(100)$ PeV, matching the energy range of

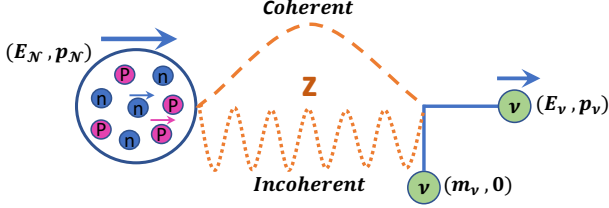


FIG. 1. Schematic diagram showing the $C\nu B$ boosted by UHECR. A nucleus \mathcal{N} with energy E_N scatters off a $C\nu B$, boosting its energy to E_ν . At a small momentum transfer, the wavelength of the Z boson is comparable to or larger than the nucleus, and coherent scattering (orange dashed line) dominates. At a large momentum transfer, the individual nucleons inside a nucleus are resolved by the Z boson, and incoherent scattering (orange dotted line) becomes important.

KM3-230213A, which suggests that KM3-230213A event may be originated from the relic neutrinos boosted by UHECR.

Cross Sections. As shown in Fig. 1, UHECR nuclei scattering off the $C\nu B$ consist of two channels: the coherent elastic neutrino-nucleus scattering and incoherent scattering [32]. Similar to the dark matter-nucleus scattering in Ref. [33–35], the total differential cross section can be written as the sum of two contributions [32], i.e.,

$$\frac{d\sigma^{\nu\mathcal{N}_i}}{dE_\nu} = \frac{d\sigma_{\text{coh}}^{\nu\mathcal{N}_i}}{dE_\nu} + \frac{d\sigma_{\text{incoh}}^{\nu\mathcal{N}_i}}{dE_\nu}, \quad (1)$$

where E_ν is the energy of the boosted $C\nu B$. At a small momentum transfer, in which the Z boson's wavelength is comparable to the nuclear radius, the relic neutrino interacts coherently with the entire nucleus, and the differential cross section in the laboratory frame is

$$\frac{d\sigma_{\text{coh}}^{\nu\mathcal{N}_i}}{dE_\nu} = \frac{2G_F^2 m_\nu}{\pi} Q_{W,i}^2 \left(1 - \frac{E_\nu}{E_{\mathcal{N}_i}} - \frac{m_{\mathcal{N}_i}^2 E_\nu}{2m_\nu E_{\mathcal{N}_i}^2} \right) F^2(q^2), \quad (2)$$

where \mathcal{N}_i is the nucleus with mass $m_{\mathcal{N}_i}$ and energy $E_{\mathcal{N}_i}$, m_ν is the neutrino mass, $q = \sqrt{2m_\nu E_\nu}$ is the momentum transfer, $F(q^2)$ is the nuclear form factor [36], $Q_{W,i} = Z_i g_V^p + N_i g_V^n$ is the nuclear weak charge with Z_i (N_i) being the proton (neutron) numbers of \mathcal{N}_i , and $g_V^{p,n}$ being the vector coupling constants. All cross-sections are summed over neutrinos and antineutrinos, taking $d\sigma^{\nu\mathcal{N}_i}/dE_\nu \equiv (d\sigma^{\nu\mathcal{N}_i}/dE_\nu + d\sigma^{\bar{\nu}\mathcal{N}_i}/dE_\nu)$ hereinafter. The derivation of the coherent cross section is provided in Section A of the Supplemental Material.

At a high momentum transfer, the Z boson resolves individual nucleons within the nucleus, which leads to incoherent scattering. The cross section can be approximated as a linear superposition of neutrino-nucleon scatterings. In the laboratory frame, the incoherent cross section is

$$\frac{d\sigma_{\text{incoh}}^{\nu\mathcal{N}_i}}{dE_\nu} = \left[Z_i \frac{d\sigma_{\text{ES}}^{\nu p}}{dE_\nu} + N_i \frac{d\sigma_{\text{ES}}^{\nu n}}{dE_\nu} \right] (1 - F^2(q^2)). \quad (3)$$

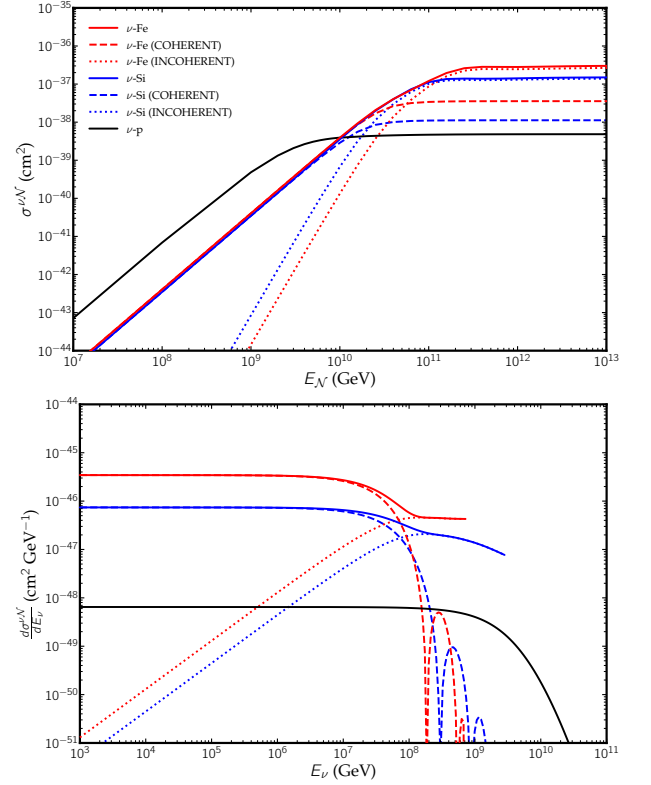


FIG. 2. Upper panel: The total neutrino-nucleus scattering cross section as a function of UHECR energy E_N for $m_\nu = 0.1$ eV. Lower panel: The differential scattering cross section as a function of boosted neutrino energy E_ν for $E_N = 100$ EeV. In both panels, red, blue, and gray solid lines represent the cross section for $C\nu B$ boosted by iron (Fe), silicon (Si), and protons (p), respectively. The dashed (dotted) lines denote the coherent (incoherent) contributions.

The differential cross section of neutrinos scattering on nucleons (denoted N) within the heavy nuclei is taken from the standard elastic scattering (ES) process [2, 14]:

$$\frac{d\sigma_{\text{ES}}^{\nu N}}{dE_\nu} = \frac{2G_F^2 m_N m_{\mathcal{N}}^4}{\pi(s - m_N^2)^2} \left[A_N(q^2) + C_N(q^2) \frac{(s - u)^2}{m_N^4} \right], \quad (4)$$

where m_N is the nucleon mass, $E_N = E_{\mathcal{N}_i}/A_i$ is approximately the nucleon energy, the Mandelstam variables $s \approx 2m_\nu E_N + m_N^2$, $t = -q^2 \approx -2m_\nu E_\nu$, and $u \approx m_N^2 - 2m_\nu(E_N - E_\nu)$, and the coefficients $A_N(q^2)$ and $C_N(q^2)$ depend on the momentum transfer q and the nucleon electromagnetic and axial form factors. We have checked that Eq. (3) and Eq. (4) are consistent with Eq. (46) in Ref. [32]; see Section A of the Supplemental Material for more details.

To illustrate the coherent and incoherent contributions to the cross section for different UHECR nuclei, we show the total cross section as a function of UHECR energy E_N for proton (p), silicon (Si), and iron (Fe) in the upper panel of Fig. 2 for $m_\nu = 0.1$ eV. We see that for $E_N \lesssim 10$ EeV, the proton elastic scattering cross section

dominates, while for E_N above ~ 10 EeV, heavier nuclei like Si and Fe exhibit larger cross sections. As E_N increases, the cross section curve reaches a plateau because the nucleon form factors $A_N(q^2)$ and $C_N(q^2)$ approach zero at very large momentum transfers q . For heavier nuclei with larger mass numbers, the suppression of the nucleon form factor occurs at higher energies since each nucleon carrying a fraction $1/A$ of the nucleus's energy E_N . The lower panel of Fig. 2 shows the differential cross section as a function of boosted neutrino energy E_ν for $E_N = 100$ EeV. Since $q = \sqrt{2m_\nu E_\nu}$, from Eq. (2), we see that coherent scattering dominates at small E_ν where $F^2(q^2) \approx 1$ and $d\sigma_{\text{coh}}/dE_\nu \propto N_i^2$. From Eq. (3), we see that incoherent scattering dominates at large E_ν where $F^2(q^2) \approx 0$ and $d\sigma_{\text{incoh}}/dE_\nu \propto A_i$. For $E_\nu \lesssim 10^8$ GeV, the differential cross-section of Fe is approximately two orders of magnitude larger than the proton elastic scattering cross section, reflecting the coherent enhancement in neutrino-nucleus scattering. Furthermore, there is a cutoff for E_ν for a given E_N , and the cutoff of heavier nuclei occurs at a lower E_ν , since the maximum boosted neutrino energy $E_\nu^{\text{max}} = E_{N_i}^2 / (E_{N_i} + m_{N_i}^2 / 2m_\nu)$ decreases as the nuclear mass m_{N_i} increases.

Boosted CνB flux. UHECR travel vast distances from their sources to the Earth, and scatter with CνB along their path, which leads to a diffuse flux of boosted neutrinos at very high energies. The differential flux of the boosted CνB at Earth can be written as

$$\frac{d\phi_\nu}{dE_\nu} = \sum_{i,j} \int_{z_{\min}}^{z_{\max}} dz \frac{c}{H(z)} f(z) \eta n_{\nu_j} (1+z)^3 \times \int_0^\infty dE_{N_i} \frac{d\sigma^{\nu N_i}}{dE'_\nu} \frac{d\phi_{N_i}}{dE_{N_i}} \Theta[E_\nu^{\text{max}} - E'_\nu], \quad (5)$$

where i and j are the indexes for the CR nuclei type and neutrino mass, respectively. n_{ν_j} is the present CνB number density per flavor. η is an overdensity factor. $H(z) = H_0 \sqrt{\Omega_m(1+z)^3 + \Omega_\Lambda}$ is the Hubble rate at redshift z , with Λ CDM parameters $c/H_0 = 1.1267 \times 10^{28}$ cm, $\Omega_m = 0.315$, and $\Omega_\Lambda = 0.685$ [37]. $f(z)$ is the redshift evolution of the CR source with the redshift integral spanning from $z_{\min} = 0$ to $z_{\max} = 6$ [38]. We use the cosmic star formation rate (SFR) distribution in the main text; see the discussion of other distributions in Section B of the Supplemental Material. Here, $d\phi_{N_i}/dE_{N_i}$ is the intergalactic UHECR flux. In general, CR require sufficient energy to escape magnetic confinement in their host galaxies [39]. Composition and anisotropy data mark the transition between Galactic and extragalactic CR at the second knee, around 5×10^8 GeV [40]. We use the Hillas model [41] to parameterize the extragalactic UHECR flux at $E_{N_i} > 5 \times 10^8$ GeV, with details given in Section B of the Supplemental Material.

The differential cross section $d\sigma^{\nu N_i}/dE'_\nu$ depends on the CR energy E_{N_i} and the neutrino energy $E'_\nu = E_\nu(1+z)$ at redshift z . Note that our Eq. (5) differs from

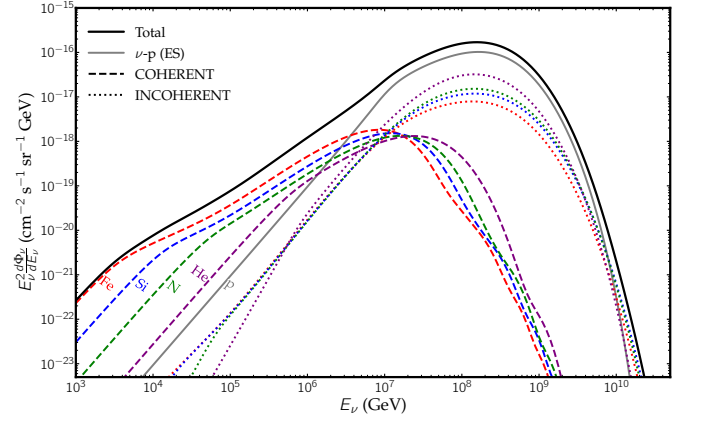


FIG. 3. The boosted CνB flux as a function of neutrino energy E_ν at Earth. Contributions from different CR elements are shown for comparison. Different colors represent various CR elements, with dashed and dotted lines indicating coherent and incoherent contributions, the gray line showing the proton ES contribution, and the black line depicting the total flux. Here we use the SFR model for the CR source evolution with $\eta = 1$ and $m_1 = 0.1$ eV.

Eq.(1) in Ref. [15], which uses $\sigma/E_\nu^{\text{max}}$ to approximate the differential neutrino-proton scattering cross section $d\sigma^{\nu N}/dE_\nu$. At high energies, $d\sigma^{\nu N}/dE_\nu$ is suppressed by nucleon form factors, whereas this suppression is not present if $\sigma/E_\nu^{\text{max}}$ is used, which will lead to an overestimation of the cross section and boosted neutrino flux; see Section C of the Supplemental Material for detailed comparison of the two cross sections.

The relative contributions of different UHECR elements to the boosted CνB flux at Earth is shown in Fig. 3 for $m_1 = 0.1$ eV. For the neutrino mass, we assume the normal ordering with mass-squared differences $\Delta m_{21}^2 = 7.42 \times 10^{-5} \text{ eV}^2$ and $\Delta m_{31}^2 = 2.51 \times 10^{-3} \text{ eV}^2$ [42]; see Section D of the Supplemental Material for different lightest neutrino masses and the case of the inverted ordering. From Fig. 3, we see that coherent scattering dominates at $E_\nu \lesssim 10^7$ GeV, with heavier nucleus has a larger coherent enhancement. For $E_\nu \gtrsim 10^7$ GeV, proton ES dominates, and the contribution from incoherent scattering of heavy nuclei is also significant.

Constraints on the overdensity. In the upper panel of Fig. 4, we show the boosted CνB flux for different lightest neutrino masses with an overdensity $\eta = 10^8$. We also compare the boosted CνB flux with the current high energy neutrino data and sensitivity curves of various observatories. The boosted CνB flux has a peak of $\sim \mathcal{O}(200 \text{ PeV})$, which can be probed at IC and Pierre Auger. We use IC and Pierre Auger to constrain the overdensity η of the CνB. The expected number of events from the boosted CνB is given by

$$n_{\text{events}} = 4\pi T \int_{E_{\min}}^{E_{\max}} dE_\nu \frac{d\phi_\nu}{dE_\nu}(\eta, m_1) A_{\text{eff}}(E_\nu), \quad (6)$$

where T is the data-taking time of 12.6 yr and 9.7 yr for IC [43] and Pierre Auger [44], respectively. $A_{\text{eff}}(E_\nu)$ is the energy-dependent effective area for all flavors taken from Ref. [45]. For IC, three neutrino events are observed at PeV energies [46–49]. We conservatively take the three events as the background, and the 90% CL Feldman-Cousins upper limit is obtained from $n_{\text{events}}^{\text{IC}} < 1.08$. For Pierre Auger, the Feldman-Cousins upper limit is set by $n_{\text{events}}^{\text{PA}} < 2.39$ which takes account of the uncertainties in the exposure [50].

The lower panel of Fig. 4 presents the 90% CL upper limits on the overdensity η as a function of the lightest neutrino mass for the normal ordering (see Section D of the Supplemental Material for the case of the inverted ordering). At $m_1 = 0.01$ eV, IceCube constrains $\eta < 5.4 \times 10^7$, while $\eta < 8.5 \times 10^8$ results from Pierre Auger. For m_1 below 0.01 eV, the constraints become independent of m_1 as the dominant contributions arise from heavier masses m_2 and m_3 . As the lightest neutrino masses increases, the constraints on η become more stringent. At $m_1 = 0.1$ eV, the bounds from IC and Pierre Auger can reach $\eta < 4.2 \times 10^6$ and 6.2×10^7 , respectively. Note that both IC and Pierre Auger set a stronger constraint than the current KATRIN upper limit of $\eta < 9.7 \times 10^{10}$ from relic neutrino capture reaction [11].

With the enhanced sensitivity of upcoming telescopes such as IceCube-Gen2 [43], Trinity-18 [58], RNO-G [59], TAMBO [60], POEMMA [61], and GRAND [62], detection of the boosted $C\nu B$ may become possible, providing direct evidence of the existence of relic neutrinos. However, distinguishing the boosted $C\nu B$ signal from background neutrinos, such as astrophysical and cosmogenic neutrinos, remains a significant challenge. As shown in the upper panel of Fig. 4, these background neutrinos exhibit characteristic energy spectra that differ from the boosted $C\nu B$, enabling potential discrimination with increased statistics. In addition, astrophysical and cosmogenic neutrinos are often accompanied by cascaded gamma-ray emission in the GeV to TeV range [63], detectable via multimessenger observations with imaging air Cherenkov telescopes and air-shower gamma-ray observatories. Astrophysical neutrinos may also be associated with signatures like gravitational waves from neutron star mergers, and such multimessenger correlations could help rule out the boosted $C\nu B$ hypothesis. Conversely, if no electromagnetic or gravitational-wave counterparts are observed, this absence, combined with energy spectrum analysis, could strengthen the case for identifying the neutrinos as boosted $C\nu B$.

Recently, the KM3NeT collaboration reported a record-breaking event, KM3-230213A, detected by the ARCA detector with an energy of 220^{+570}_{-110} PeV [31]. The energy aligns with the peak of the boosted $C\nu B$ flux as shown in the upper panel of Fig. 4, and this coincidence allows us to entertain the possibility of explain-

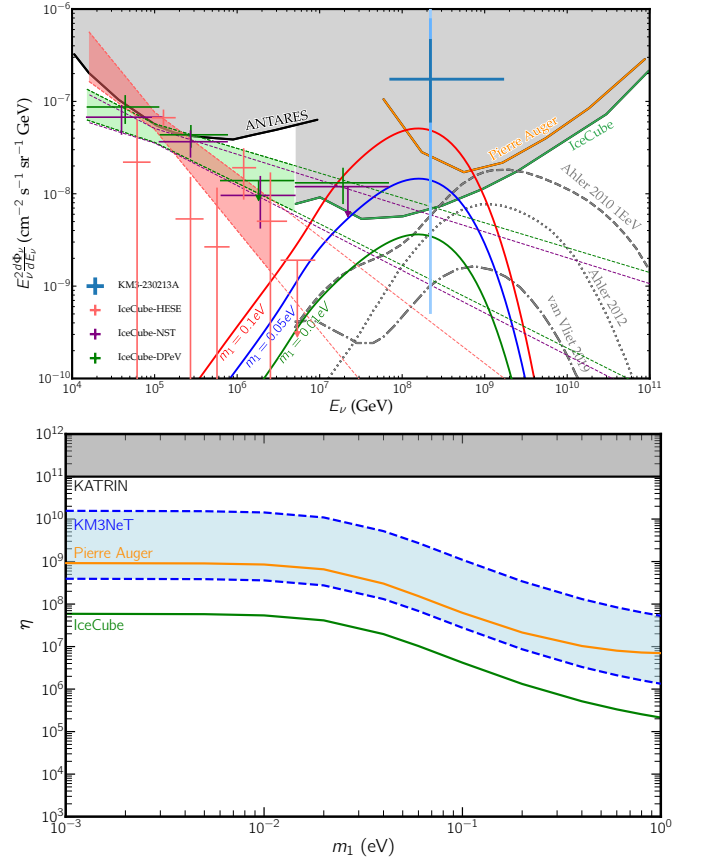


FIG. 4. Upper panel: The all-flavor boosted $C\nu B$ flux as a function of neutrino energy E_ν for different lightest neutrino masses m_1 , compared to experimental limits and data. Red, blue, and green solid lines represent the flux for $m_1 = 0.1$ eV, 0.05 eV, and 0.01 eV, respectively. Varying shades of blue indicate the 1σ , 2σ , and 3σ ranges for KM3-230213A at KM3NeT. Also shown are limits on the diffuse cosmogenic flux from IceCube (90% CL) [43, 46], Pierre Auger (90% CL) [44], and ANTARES (95% CL) [51], alongside the measured astrophysical neutrino spectrum from IceCube analysis of high-energy starting events (HESE) [52], northern sky tracks (NST) [53], and downgoing PeV events (DPeV) [54]. Various cosmogenic neutrino flux models [55–57] are also shown as gray curves for comparison. The overdensity η in the upper panel is set to 10^8 . Lower panel: Constraints on the $C\nu B$ overdensity η as a function of the lightest neutrino mass m_1 . The green and orange lines corresponds to the 90% CL constraints from IceCube and Pierre Auger, respectively. The blue region indicates the allowed parameter space from KM3NeT; the gray region represents the exclusion region from KATRIN at the 90% CL. We use the SFR model for the CR source evolution in both the upper and lower panels.

ing the KM3NeT event by the relic neutrinos boosted by UHECR. We also plot the 90% CL allowed region that can explain KM3-230213A in the lower panel of Fig. 4, and we see that the explanation of KM3-230213A requires an overdensity within $[3.7 \times 10^8, 1.5 \times 10^{10}]$ for $m_1 = 0.01$ eV, which is below the current KATRIN

bound. Note that the allowed region to explain the KM3Net event is in tension with the IC bound, which agrees with the 3.5σ tension between IC and KM3Net for the diffuse neutrino flux, as IceCube has a larger effective area and longer runtime [45, 64]. This tension can be alleviated in the presence of new physics scenarios such as sterile-to-active neutrino transitions under nonstandard matter effects [65], or neutrino self-interactions [66].

Summary. In this Letter, we study the diffuse flux of the $C\nu B$ boosted by UHECR in the intergalactic medium. We take account of both the coherent and incoherent scattering channels, and use energy-dependent differential cross sections to calculate the flux for different lightest neutrino masses and CR source distributions. We find that coherent scattering dominates at low momentum transfers, significantly enhancing the cross-section through collective interactions with all nucleons, while incoherent scattering becomes prominent at higher energies as individual nucleons are resolved.

Using current data from IC and Pierre Auger, we set constraints on the $C\nu B$ overdensity η . We find that for $m_1 = 0.1\text{ eV}$, the bounds from IC and Pierre Auger can reach $\eta < 4.2 \times 10^6$ and 6.2×10^7 , respectively. Since the recent observed KM3NeT event has an energy aligning with the peak of the boosted relic neutrino flux, we also entertain the possibility of explaining the KM3NeT event with the boosted $C\nu B$ origin. Future observatories, such as IceCube-Gen2 and POEMMA, may enable the first detection of the boosted $C\nu B$, and potentially distinguish it from cosmogenic neutrinos through differences in energy spectra and multimessenger observations.

ACKNOWLEDGMENTS

We thank Karl-Heinz Kampert for useful comments and suggestions. J.L. is supported by the National Natural Science Foundation of China under Grant Nos. 12275368 and the Fundamental Research Funds for the Central Universities, Sun Yat-Sen University under Grant No. 24qnpy116.

* zhangjj253@mail2.sysu.edu.cn

† asandrock@uni-wuppertal.de

‡ liaojiajun@mail.sysu.edu.cn

§ bayue@uni-wuppertal.de

- [1] Topical Conveners: K.N. Abazajian, J.E. Carlstrom, A.T. Lee, *Astropart. Phys.* **63**, 66 (2015), arXiv:1309.5383 [astro-ph.CO].
- [2] C. Giunti and C. W. Kim, *Fundamentals of Neutrino Physics and Astrophysics* (Oxford University Press, Oxford, 2007).
- [3] J. Lesgourgues, G. Mangano, G. Miele, and S. Pastor, *Neutrino cosmology* (Cambridge University Press, 2013).

- [4] E. Baracchini *et al.* (PTOLEMY), “PTOLEMY: A Proposal for Thermal Relic Detection of Massive Neutrinos and Directional Detection of MeV Dark Matter,” (2018), arXiv:1808.01892 [physics.ins-det].
- [5] PTOLEMY Collaboration, *Phys. Rev. D* **106**, 053002 (2022), arXiv:2203.11228 [hep-ph].
- [6] K. Bondarenko, A. Boyarsky, J. Pradler, and A. Sokolenko, *JCAP* **10**, 026 (2023), arXiv:2306.12366 [hep-ph].
- [7] D. McKeen, *Phys. Rev. D* **100**, 015028 (2019), arXiv:1812.08178 [hep-ph].
- [8] Z. Chacko, P. Du, and M. Geller, *Phys. Rev. D* **100**, 015050 (2019), arXiv:1812.11154 [hep-ph].
- [9] M. Nikolic, S. Kulkarni, and J. Pradler, *Eur. Phys. J. C* **82**, 650 (2022), arXiv:2008.13557 [hep-ph].
- [10] A. Y. Smirnov and X.-J. Xu, *JHEP* **08**, 170 (2022), arXiv:2201.00939 [hep-ph].
- [11] M. Aker *et al.* (KATRIN), *Phys. Rev. Lett.* **129**, 011806 (2022), arXiv:2202.04587 [nucl-ex].
- [12] T. Hara and H. Sato, *Prog. Theor. Phys.* **62**, 969 (1979).
- [13] T. Hara and H. Sato, *Prog. Theor. Phys.* **65**, 477 (1981).
- [14] M. Císcar-Monsalvatje, G. Herrera, and I. M. Shoemaker, *Phys. Rev. D* **110**, 063036 (2024), arXiv:2402.00985 [hep-ph].
- [15] G. Herrera, S. Horiuchi, and X. Qi, *Phys. Rev. D* **111**, 023016 (2025), arXiv:2405.14946 [hep-ph].
- [16] A. G. De Marchi, A. Granelli, J. Nava, and F. Sala, *Phys. Rev. D* **111**, 023023 (2025), arXiv:2405.04568 [hep-ph].
- [17] A. A. Halim *et al.* (Pierre Auger), *JCAP* **05**, 024 (2023), arXiv:2211.02857 [astro-ph.HE].
- [18] D. Ehlert, A. van Vliet, F. Oikonomou, and W. Winter, *JCAP* **02**, 022 (2024), arXiv:2304.07321 [astro-ph.HE].
- [19] E. Armengaud, G. Sigl, and F. Miniati, *Phys. Rev. D* **72**, 043009 (2005), arXiv:astro-ph/0412525.
- [20] D. Allard, N. G. Busca, G. Decerprit, A. V. Olinto, and E. Parizot, *JCAP* **10**, 033 (2008), arXiv:0805.4779 [astro-ph].
- [21] K. Arisaka, G. B. Gelmini, M. D. Healy, O. E. Kalashev, and J. Lee, *JCAP* **12**, 002 (2007), arXiv:0709.3390 [astro-ph].
- [22] W. D. Apel *et al.*, *Astropart. Phys.* **47**, 54 (2013), arXiv:1306.6283 [astro-ph.HE].
- [23] R. U. Abbasi *et al.* (Telescope Array), *Phys. Rev. D* **99**, 022002 (2019), arXiv:1808.03680 [astro-ph.HE].
- [24] D. Z. Freedman, *Phys. Rev. D* **9**, 1389 (1974).
- [25] COHERENT Collaboration, *Science* **357**, 1123 (2017), arXiv:1708.01294 [nucl-ex].
- [26] COHERENT Collaboration, *Phys. Rev. Lett.* **126**, 012002 (2021), arXiv:2003.10630 [nucl-ex].
- [27] COHERENT Collaboration, *Phys. Rev. Lett.* (2024), arXiv:2406.13806 [hep-ex].
- [28] XENON Collaboration, *Phys. Rev. Lett.* **133**, 191002 (2024), arXiv:2408.02877 [nucl-ex].
- [29] PandaX Collaboration, *Phys. Rev. Lett.* **133**, 191001 (2024), arXiv:2407.10892 [hep-ex].
- [30] N. Ackermann, H. Bonet, A. Bonhomme, *et al.*, “First observation of reactor antineutrinos by coherent scattering,” (2025), preprint, arXiv:2501.05206 [hep-ex].
- [31] S. Aiello *et al.* (KM3NeT), *Nature* **638**, 376 (2025).
- [32] V. A. Bednyakov and D. V. Naumov, *Phys. Rev. D* **98**, 053004 (2018), arXiv:1806.08768 [hep-ph].
- [33] V. A. Bednyakov, “On underestimation of the inelastic interactions in the direct dark matter search,” (2023), arXiv:2305.02050 [hep-ph].

- [34] B. Betancourt Kamenetskaia, M. Fujiwara, A. Ibarra, and T. Toma, Phys. Lett. B **864**, 139425 (2025), arXiv:2501.12117 [hep-ph].
- [35] S.-F. Ge and O. Titov, Phys. Rev. D **110**, 055003 (2024), arXiv:2405.05728 [hep-ph].
- [36] S. Klein and J. Nystrand, Phys. Rev. C **60**, 014903 (1999), arXiv:hep-ph/9902259 [hep-ph].
- [37] Particle Data Group, Phys. Rev. D **110**, 030001 (2024).
- [38] A. M. Hopkins and J. F. Beacom, Astrophys. J. **651**, 142 (2006), arXiv:astro-ph/0601463 [astro-ph].
- [39] R. Alves Batista *et al.*, Front. Astron. Space Sci. **6**, 23 (2019), arXiv:1903.06714 [astro-ph.HE].
- [40] M. Kachelriess and D. V. Semikoz, Prog. Part. Nucl. Phys. **109**, 103710 (2019), arXiv:1904.08160 [astro-ph.HE].
- [41] A. M. Hillas, J. Phys. G **31**, R95 (2005).
- [42] I. Esteban, M. C. Gonzalez-Garcia, M. Maltoni, T. Schwetz, and A. Zhou, JHEP **09**, 178 (2020), arXiv:2007.14792 [hep-ph].
- [43] M. Meier (IceCube), in *58th Rencontres de Moriond on Very High Energy Phenomena in the Universe* (2024) arXiv:2409.01740 [astro-ph.HE].
- [44] A. Aab *et al.* (Pierre Auger), JCAP **10**, 022 (2019), arXiv:1906.07422 [astro-ph.HE].
- [45] O. Adriani *et al.* (KM3NeT), (2025), arXiv:2502.08173 [astro-ph.HE].
- [46] R. Abbasi *et al.* (IceCube), (2025), arXiv:2502.01963 [astro-ph.HE].
- [47] M. G. Aartsen *et al.* (IceCube), Nature **591**, 220 (2021), [Erratum: Nature 592, E11 (2021)], arXiv:2110.15051 [hep-ex].
- [48] Icecube Collaboration, GRB Coordinates Network **24028**, 1 (2019).
- [49] M. G. Aartsen *et al.* (IceCube), Astrophys. J. **833**, 3 (2016), arXiv:1607.08006 [astro-ph.HE].
- [50] A. Aab *et al.* (Pierre Auger), Phys. Rev. D **91**, 092008 (2015), arXiv:1504.05397 [astro-ph.HE].
- [51] A. Albert *et al.* (ANTARES), JCAP **08**, 038 (2024), arXiv:2407.00328 [astro-ph.HE].
- [52] R. Abbasi *et al.* (IceCube), Phys. Rev. D **104**, 022002 (2021), arXiv:2011.03545 [astro-ph.HE].
- [53] R. Abbasi *et al.*, Astrophys. J. **928**, 50 (2022), arXiv:2111.10299 [astro-ph.HE].
- [54] R. Abbasi *et al.* (IceCube), (2025), arXiv:2502.19776 [astro-ph.HE].
- [55] M. Ahlers, L. A. Anchordoqui, M. C. Gonzalez-Garcia, F. Halzen, and S. Sarkar, Astropart. Phys. **34**, 106 (2010), arXiv:1005.2620 [astro-ph.HE].
- [56] M. Ahlers and F. Halzen, Phys. Rev. D **86**, 083010 (2012), arXiv:1208.4181 [astro-ph.HE].
- [57] A. van Vliet, R. Alves Batista, and J. R. Hörandel, Phys. Rev. D **100**, 021302 (2019), arXiv:1901.01899 [astro-ph.HE].
- [58] A. N. Otte, A. M. Brown, A. D. Falcone, M. Mariotti, and I. Taboada, PoS **ICRC2019**, 976 (2020), arXiv:1907.08732 [astro-ph.IM].
- [59] O. Scholten, RNO-G Collaboration, *et al.*, in *9th International Workshop on Acoustic and Radio EeV Neutrino Detection Activities, ARENA 2022* (Proceedings of Science, 2023).
- [60] A. Romero-Wolf *et al.*, in *Latin American Strategy Forum for Research Infrastructure* (2020) arXiv:2002.06475 [astro-ph.IM].
- [61] A. V. Olinto *et al.* (POEMMA), JCAP **06**, 007 (2021), arXiv:2012.07945 [astro-ph.IM].
- [62] O. Martineau-Huynh *et al.* (GRAND), EPJ Web Conf. **135**, 02001 (2017), arXiv:1702.01395 [astro-ph.IM].
- [63] K. Fang, F. Halzen, and D. Hooper, Astrophys. J. Lett. **982**, L16 (2025), arXiv:2502.09545 [astro-ph.HE].
- [64] S. W. Li, P. Machado, D. Naredo-Tuero, and T. Schwemmerberger, “Clash of the Titans: ultra-high energy KM3NeT event versus IceCube data,” (2025), arXiv:2502.04508 [astro-ph.HE].
- [65] V. Brdar and D. S. Chattopadhyay, (2025), arXiv:2502.21299 [hep-ph].
- [66] Y. He, J. Liu, X.-P. Wang, and Y.-M. Zhong, (2025), arXiv:2504.20163 [hep-ph].
- [67] M. Lindner, W. Rodejohann, and X.-J. Xu, JHEP **03**, 097 (2017), arXiv:1612.04150 [hep-ph].
- [68] J. A. Formaggio and G. P. Zeller, Rev. Mod. Phys. **84**, 1307 (2012), arXiv:1305.7513 [hep-ex].
- [69] H. Gao and M. Vanderhaeghen, Rev. Mod. Phys. **94**, 015002 (2022), arXiv:2105.00571 [hep-ph].
- [70] Extended Twisted Mass Collaboration, Phys. Rev. D **109**, 034503 (2024).
- [71] T. K. Gaisser, Astropart. Phys. **35**, 801 (2012), arXiv:1111.6675 [astro-ph.HE].
- [72] T. K. Gaisser, T. Stanev, and S. Tilav, Front. Phys. (Beijing) **8**, 748 (2013), arXiv:1303.3565 [astro-ph.HE].
- [73] G. Giacinti, M. Kachelriess, D. V. Semikoz, and G. Sigl, JCAP **07**, 031 (2012), arXiv:1112.5599 [astro-ph.HE].
- [74] A. M. Hopkins and J. F. Beacom, The Astrophysical Journal **651**, 142 (2006).
- [75] J. V. Wall, C. Jackson, P. Shaver, I. Hook, and K. Kellermann, Astronomy & Astrophysics **434**, 133 (2005).
- [76] G.-X. Lan, J.-J. Wei, H.-D. Zeng, Y. Li, and X.-F. Wu, Mon. Not. Roy. Astron. Soc. **508**, 52 (2021), arXiv:2109.00766 [astro-ph.HE].
- [77] D. Bardhan, S. Bhowmick, D. Ghosh, A. Guha, and D. Sachdeva, Phys. Rev. D **107**, 015010 (2023), arXiv:2208.09405 [hep-ph].

SUPPLEMENTAL MATERIAL

Section A. Cross sections

Kinematics. The $C\nu B$ have extremely low energy, and can be treated as at rest in the laboratory frame. To analyze the scattering of a CR nucleus \mathcal{N}_i off a relic neutrino at rest, we define the four-momenta as follows: $P_\nu = \{m_\nu, 0\}$ for the incoming neutrino and $P'_\nu = \{E_\nu, \vec{p}_\nu\}$ for the outgoing neutrino; $K_{\mathcal{N}} = \{E_{\mathcal{N}}, \vec{p}_{\mathcal{N}}\}$ for the initial nucleus and $K'_{\mathcal{N}} = \{E'_{\mathcal{N}}, \vec{p}'_{\mathcal{N}}\}$ for the final nucleus. Given the energy scales involved, we apply the approximation $E_{\mathcal{N}_i} \gg m_{\mathcal{N}_i} \gg m_\nu$, which holds for UHECR interactions. Using energy-momentum conservation, the Mandelstam variables are approximated as $s \approx 2m_\nu E_{\mathcal{N}} + m_{\mathcal{N}}^2$, $t = -Q^2 \approx -2m_\nu E_\nu$, and $u \approx m_{\mathcal{N}}^2 - 2m_\nu(E_{\mathcal{N}} - E_\nu)$. The maximum energy of the scattered neutrino, E_ν^{\max} , is given by

$$E_\nu^{\max}(E_{\mathcal{N}_i}) = \frac{E_{\mathcal{N}_i}^2}{E_{\mathcal{N}_i} + m_{\mathcal{N}_i}^2/(2m_\nu)} \approx \begin{cases} E_{\mathcal{N}_i} & \text{if } E_{\mathcal{N}_i} \gg \frac{m_{\mathcal{N}_i}^2}{2m_\nu}, \\ \frac{2m_\nu E_{\mathcal{N}_i}^2}{m_{\mathcal{N}_i}^2} & \text{if } E_{\mathcal{N}_i} \ll \frac{m_{\mathcal{N}_i}^2}{2m_\nu}, \end{cases} \quad (7)$$

Coherent neutrino-nucleus scattering cross sections. For coherent scattering, the axial-vector interactions can be neglected, and we assume that the atomic nucleus is a scalar particle with no spin for simplicity [67]. Thus, neutrinos and antineutrinos exhibit identical scattering amplitudes. The scattering amplitude for the process $\nu + \mathcal{N}_i \rightarrow \nu + \mathcal{N}_i$ is given by [67]

$$i\mathcal{M} = i\frac{\sqrt{2}}{2}G_F Q_W F(q^2)(K_{\mathcal{N}_i} + K'_{\mathcal{N}_i})^\mu \bar{v}(P_\nu)\gamma_\mu(1 - \gamma^5)v(P'_\nu), \quad (8)$$

with the amplitude squared

$$|\mathcal{M}|^2 = 32G_F^2 Q_W^2 F^2(q^2)m_\nu^2 E_{\mathcal{N}_i}^2 \left(1 - \frac{E_\nu}{E_{\mathcal{N}_i}} - \frac{m_\nu^2 E_\nu}{2E_{\mathcal{N}_i}^2 m_{\mathcal{N}_i}}\right), \quad (9)$$

where the nuclear weak charge is $Q_{W,i} = Z_i g_V^p + N_i g_V^n$, with $g_V^p = \frac{1}{2} - 2\sin^2 \theta_W$ and $g_V^n = -\frac{1}{2}$, and $\sin^2 \theta_W = 0.231$ [37]. The differential scattering cross section for neutrino-nucleus interactions is expressed as

$$\frac{d\sigma}{dQ^2} = \frac{1}{16\pi} \frac{|\mathcal{M}|^2}{\lambda(s, m_{\mathcal{N}_i}^2, m_\nu^2)}, \quad (10)$$

where $\lambda(s, m_{\mathcal{N}_i}^2, m_\nu^2) = s^2 + m_{\mathcal{N}_i}^4 + m_\nu^4 - 2sm_{\mathcal{N}_i}^2 - 2sm_\nu^2 - 2m_{\mathcal{N}_i}^2 m_\nu^2 \approx (s - m_{\mathcal{N}_i}^2)^2$. In the laboratory frame, the differential cross-section for the sum of neutrino and antineutrino contributions to neutrino-nucleus coherent scattering is

$$\frac{d\sigma_{\text{coh}}^{\nu\mathcal{N}_i}}{dE_\nu} = \frac{2G_F^2 m_\nu^2}{\pi} F^2(q^2) Q_{W,i}^2 \left(1 - \frac{E_\nu}{E_{\mathcal{N}_i}} - \frac{m_{\mathcal{N}_i}^2 E_\nu}{2m_\nu E_{\mathcal{N}_i}^2}\right), \quad (11)$$

Elastic neutrino-nucleon scattering cross section. The elastic scattering cross section for a nucleon N scattering off a (anti)neutrino in the laboratory frame, where the initial (anti)neutrino is at rest, has been derived in prior work [2, 16, 68]. We summarize the differential cross section as follows

$$\frac{d\sigma_{\text{ES}}^{\nu N}}{dE_\nu} = \frac{2G_F^2 m_\nu m_N}{\pi(s - m_N^2)^2} \left[A(q^2) \pm B(q^2) \frac{s - u}{m_N^2} + C(q^2) \frac{(s - u)^2}{m_N^4} \right], \quad (12)$$

where the \pm sign is positive for neutrinos and negative for antineutrinos, reflecting the differing contributions of the axial-vector terms. The coefficients $A(q^2)$, $B(q^2)$, and $C(q^2)$ depend on the momentum transfer q , and they are given by

$$A_N(q^2) = \frac{q^2}{m_N^2} \left\{ \left(1 + \frac{q^2}{4m_N^2}\right) (G_A^{ZN})^2 - \left(1 - \frac{q^2}{4m_N^2}\right) \left[(F_1^{ZN})^2 - \frac{q^2}{4m_N^2} (F_2^{ZN})^2 \right] + \frac{q^2}{m_N^2} \frac{F_1^{ZN} F_2^{ZN}}{4} \right\}, \quad (13)$$

$$B_N(q^2) = \frac{q^2}{m_N^2} G_A^{ZN} (F_1^{ZN} + F_2^{ZN}), \quad (14)$$

$$C_N(q^2) = \frac{1}{4} \left[(G_A^{ZN})^2 + (F_1^{ZN})^2 + \frac{q^2}{4m_N^2} (F_2^{ZN})^2 \right], \quad (15)$$

where F_1^{ZN} and F_2^{ZN} are the Dirac and Pauli electromagnetic form factors for the weak neutral currents, and they are defined as $F_i^{ZN} = \pm \frac{1}{2}(F_i^p - F_i^n) - 2\sin^2 \theta_W F_i^N$, with the $+$ ($-$) sign for $N = p(n)$. The axial form factor is

$G_A^{ZN} = \pm(1/2)G_A$, with the same sign convention. The electric and magnetic form factors are defined as [2]:

$$G_E^N(q^2) = F_1^N(q^2) - \frac{q^2}{4m_N^2} F_2^N(q^2), \quad G_M^N(q^2) = F_1^N(q^2) + F_2^N(q^2), \quad (16)$$

with q^2 -dependence given by $G_{E,M}^N(q^2) = G_{E,M}^N(0)(1+q^2/\Lambda_{E,M}^2)^{-2}$, where $\Lambda_{E,M} \simeq 0.8 \text{ GeV}$, and $G_A(q^2) = G_A(0)(1+q^2/m_A^2)^{-2}$, with $G_A(0) \simeq 1.245$ and $m_A \simeq 1.17 \text{ GeV}$ [69, 70]. At zero momentum transfer ($q^2 = 0$), these form factors become $G_E^p(0) = 1$, $G_E^n(0) = 0$, $G_M^p(0) = \mu_p/\mu_N$, and $G_M^n(0) = \mu_n/\mu_N$, where $\mu_p/\mu_N = 2.79$ and $\mu_n/\mu_N = -1.91$ [37] are the magnetic moments of the proton and neutron, respectively.

Incoherent neutrino-nucleus scattering cross section. As the momentum transfer q increases, the nucleons bound within the nucleus \mathcal{N}_i are resolved, and the neutrino-nucleus scattering cross-section can be approximated as sum of contributions from individual nucleons, i.e.,

$$\frac{d\sigma_{\text{incoh}}^{\nu\mathcal{N}_i}}{dE_\nu} = \left[Z_i \frac{d\sigma_{\text{ES}}^{\nu p}}{dE_\nu} + N_i \frac{d\sigma_{\text{ES}}^{\nu n}}{dE_\nu} \right] (1 - F^2(q^2)), \quad (17)$$

where Z_i and N_i are the number of protons and neutrons in the nucleus \mathcal{N}_i , respectively. $F(q^2)$ is the nuclear form factor.

To evaluate the differential cross section in Eq. (17), we use the elastic neutrino-nucleon scattering cross section with reasonable assumptions for the form factors. For $m_\nu = 0.1 \text{ eV}$, the boosted neutrino energy peaks at $\sim \mathcal{O}(200 \text{ PeV})$, corresponding to a momentum transfer $q \approx 0.2 \text{ GeV}$. This yields $q^2/\Lambda_{E,M}^2 (q^2/m_A^2) \approx 0.06(0.03)$, hence the form factors can be approximated as $G_A(q^2) \approx G_A(0) = g_A^N$, $F_1^{ZN}(q^2) \approx F_1^{ZN}(0) = g_V^N$, and $F_2^{ZN}(q^2) \approx F_2^{ZN}(0)$. Since $B(q^2)$ changes sign between neutrinos and antineutrinos, its contribution cancels after summing over ν and $\bar{\nu}$, resulting in $B = 0$. At $q^2 \approx 0$, the coefficients simplify to

$$A_N(0) = \frac{q^2}{m_N^2} [G_A^{ZN}(0)^2 - F_1^{ZN}(0)^2], \quad C_N(0) = \frac{1}{4} [G_A^{ZN}(0)^2 + F_1^{ZN}(0)^2], \quad (18)$$

This form factor at zero momentum transfer is $G_A^{ZN}(0) = \pm \frac{1}{2} G_A(0) = g_A^N$ and $F_1^{ZN}(0) = \pm \frac{1}{2} (F_1^p(0) - F_1^n(0)) - 2 \sin^2 \theta_W F_1^N(0) = g_V^N$, giving $A_N(0) = \frac{q^2}{m_N^2} [(g_A^N)^2 - (g_V^N)^2]$ and $C_N(0) = \frac{1}{4} [(g_A^N)^2 + (g_V^N)^2]$. In the laboratory frame, the Mandelstam variables are approximated as $s \approx 2m_\nu E_N + m_N^2$ and $u \approx m_N^2 - 2m_\nu(E_N - E_\nu)$. Substituting the elastic scattering cross-section from Eq. (12) into Eq. (17), we obtain

$$\frac{d\sigma_{\text{incoh}}^{\nu\mathcal{N}_i}}{dE_\nu} = \frac{2G_F^2 m_\nu}{\pi} \left[(Z_i g_V^p{}^2 + N_i g_V^n{}^2) \left(1 - \frac{E_\nu}{E_N} - \frac{m_N^2 E_\nu}{2m_\nu E_N^2} \right) + (Z_i g_A^p{}^2 + N_i g_A^n{}^2) \left(1 - \frac{E_\nu}{E_N} + \frac{m_N^2 E_\nu}{2m_\nu E_N^2} \right) \right] (1 - F^2(q^2)), \quad (19)$$

From the derivation, it is evident that Eq. (19) is an approximation of Eq. (17) after the nucleon form factor effects are neglected.

The incoherent neutrino-nucleus scattering cross section has been studied previously in Ref. [32]. Now we demonstrate that Eq. (19) is consistent with the incoherent cross section derived in Ref. [32], which is given by

$$\frac{d\sigma_{\text{incoh}}^{\nu\mathcal{N}_i}}{dE_\nu} = g_{\text{inc}} \frac{2G_F^2 m_\nu}{\pi} \sum_{N=p,n} A^N \left[(g_L^N)^2 + (g_R^N)^2 (1-y)^2 - \frac{2g_L^N g_R^N m_N y}{s - m_N^2} \right] (1 - F^2(q^2)), \quad (20)$$

For antineutrinos, the couplings are flipped ($g_L^N \rightarrow g_R^N$, $g_R^N \rightarrow g_L^N$), and we have

$$\frac{d\sigma_{\text{incoh}}^{\bar{\nu}\mathcal{N}_i}}{dE_\nu} = g_{\text{inc}} \frac{2G_F^2 m_\nu}{\pi} \sum_{N=p,n} A^N \left[(g_R^N)^2 + (g_L^N)^2 (1-y)^2 - \frac{2g_L^N g_R^N m_N y}{s - m_N^2} \right] (1 - F^2(q^2)), \quad (21)$$

where the variable $y = \frac{(P_\nu \cdot q)}{(P_\nu \cdot K_N)} = \frac{s - m_N^2}{s} \frac{q^2}{q_{\text{max}}^2} = \frac{E_\nu}{E_N}$. The incoherent coefficient $g_{\text{inc}} \approx 1$ [32] since nuclear excitation energies ($\sim \text{keV}$) are negligible compared to $E_{N_i} \sim \mathcal{O}(\text{EeV})$. Summing over the contributions from neutrinos and antineutrinos, the differential cross section becomes

$$\begin{aligned} \frac{d\sigma_{\text{incoh}}^{\nu\mathcal{N}_i}}{dE_\nu} &= \left(\frac{d\sigma_{\text{incoh}}^{\nu\mathcal{N}_i}}{dE_\nu} + \frac{d\sigma_{\text{incoh}}^{\bar{\nu}\mathcal{N}_i}}{dE_\nu} \right) = \frac{2G_F^2 m_\nu}{\pi} \sum_{N=p,n} A^N \left[((g_L^N)^2 + (g_R^N)^2) (1 + (1-y)^2) - \frac{4g_L^N g_R^N m_N y}{s - m_N^2} \right] (1 - F^2(q^2)) \\ &= \frac{2G_F^2 m_\nu}{\pi} \left[(Z_i g_V^p{}^2 + N_i g_V^n{}^2) \left(1 - \frac{E_\nu}{E_N} - \frac{m_N^2 E_\nu}{2m_\nu E_N^2} \right) + (Z_i g_A^p{}^2 + N_i g_A^n{}^2) \left(1 - \frac{E_\nu}{E_N} + \frac{m_N^2 E_\nu}{2m_\nu E_N^2} \right) \right] (1 - F^2(q^2)), \end{aligned} \quad (22)$$

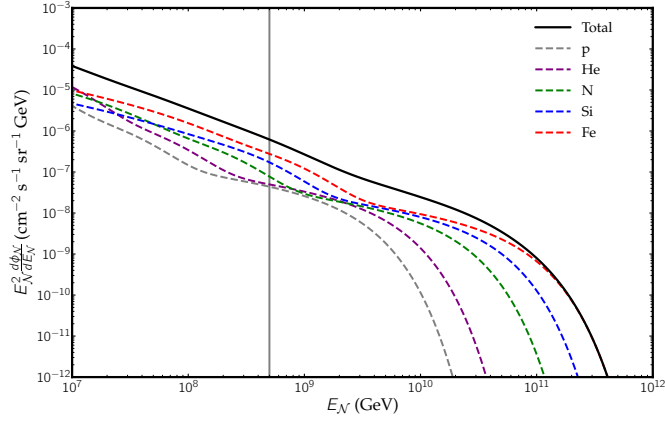


FIG. 5. Hillas cosmic ray energy spectrum for different nuclei. Different colors represent flux contributions from various cosmic ray elements, with the black solid line showing the total flux. A gray solid line marks the transition to extragalactic sources.

In the last equation, we have transformed the left- and right-handed couplings into vector and axial-vector couplings using $g_V^N = g_L^N + g_R^N$ and $g_A^N = g_L^N - g_R^N$, allowing the cross-section to be expressed in terms of $(g_V^N)^2$ and $(g_A^N)^2$, which yields Eq. (19).

As we see from the above derivation, by neglecting nucleon form factor effects, the incoherent neutrino-nucleus scattering cross section derived in this work (Eq. (19)) and that in Ref. [32](Eq. (20)) are consistent. Note that the cross section we adopted in Eq. (17) can be applied to more general scenarios, since it takes in account the nucleon form factor effect, which is critical for accurate capturing scattering dynamics at a large momentum transfer.

Section B. Cosmic ray energy spectrum and source evolution

Hillas cosmic ray energy spectrum. The CR flux is modeled by the Hillas approach [71, 72], which describes the all-particle energy spectrum as the sum over distinct CR populations. The differential flux for a nucleus of type i is given by:

$$\frac{d\phi_{N_i}}{dE_{N_i}} = \sum_{j=1}^3 a_{i,j} E_{N_i}^{-\gamma_{i,j}-1} \exp\left(-\frac{E_{N_i}}{Z_i R_{c,j}}\right), \quad (23)$$

where E_{N_i} is the energy per nucleus, Z_i is the atomic number, $R_{c,j}$ is the characteristic cutoff rigidity for population j , and $a_{i,j}$ ($\gamma_{i,j}$) is the normalization constant (spectral index), adopted from fits to observational data. Table I lists the parameters for different populations and elements (p, He, N, Si, Fe), including the cutoff rigidities $R_{c,j}$, normalization constants $a_{i,j}$ (top row per population), and integral spectral indices $\gamma_{i,j}$ (bottom row per population).

	p	He	N	Si	Fe
Pop. 1:	7860	3550	2200	1430	2120
$R_c = 4$ PV	1.66	1.58	1.63	1.67	1.63
Pop. 2:	20	20	13.4	13.4	13.4
$R_c = 30$ PV	1.4	1.4	1.4	1.4	1.4
Pop. 3:	1.7	1.7	1.14	1.14	1.14
$R_c = 2$ EV	1.4	1.4	1.4	1.4	1.4

TABLE I. Hillas model parameters for different populations and elements (p, He, N, Si, Fe) [72].

The Hillas model parameterizes the cosmic ray energy spectrum using a three population framework [41, 72], as tabulated in Table I, with the spectrum plot in Fig 5. These three populations correspond to the knee, marking the upper limit of the spectrum from CR accelerated by supernova remnants in the Milky Way, the ankle, representing the transition to extragalactic sources, and the gap between the knee and the ankle, whose origin remains uncertain. However, Ref. [40] supports the second knee, near $E_N \sim 5 \times 10^8$ GeV, as the boundary between Galactic and extragalactic CR. In Ref. [73], it was shown that a light (intermediate) Galactic CR flux leads to a dipole amplitude of order 20%, exceeding the observational limits. Thus the dominant light-intermediate contribution to the CR

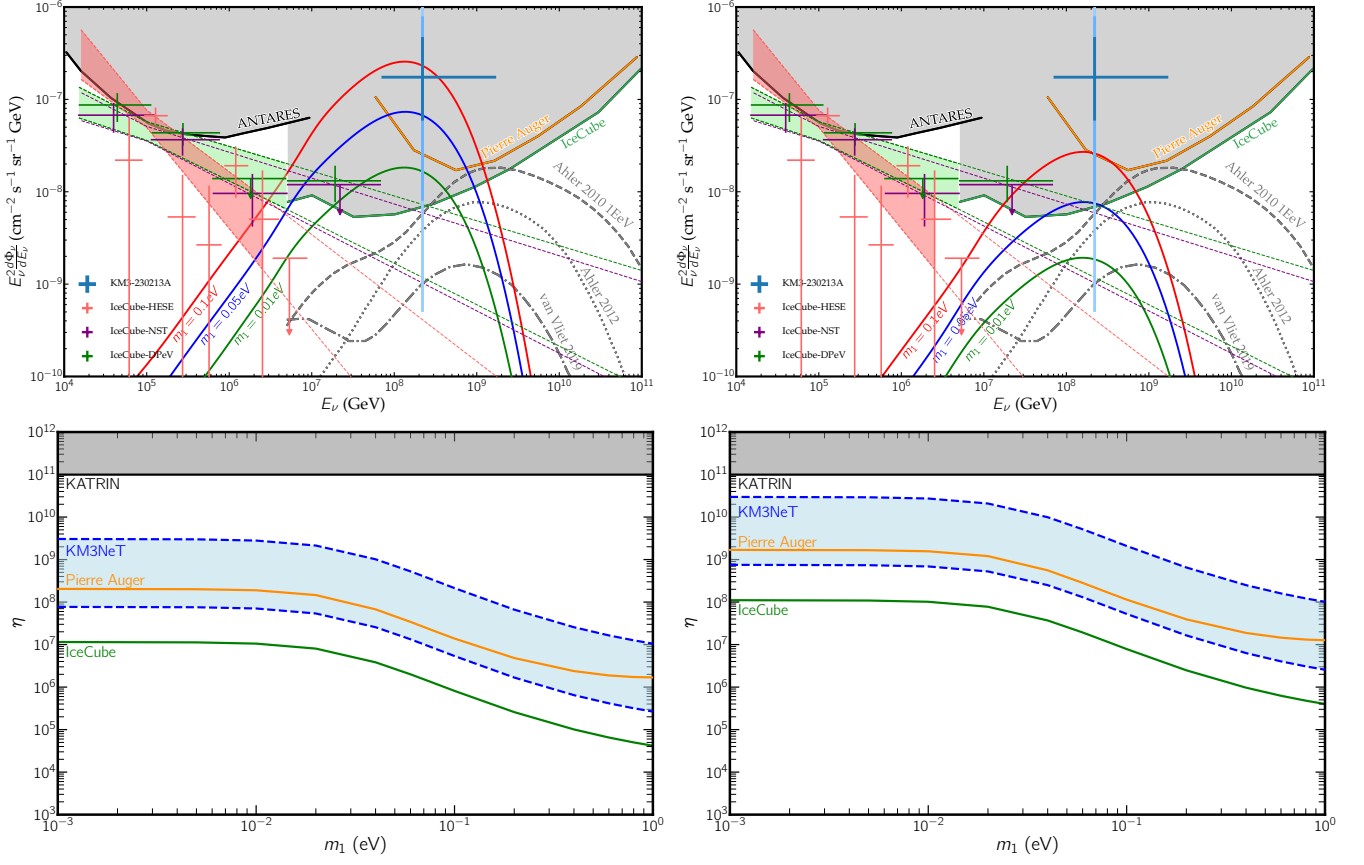


FIG. 6. Same as Fig. 4, except for showing the boosted flux calculated with the CR source distributions for GRB (left panels) and QSO (right panels).

flux above $3 \times 10^8 \text{ GeV}$ has to be extragalactic [40]. This transition energy, chosen at the upper end of the range $(1 - 5) \times 10^8 \text{ GeV}$ for consistency with observational data, aligns with composition and anisotropy measurements suggesting the Galactic contribution diminishes before this energy [40]. Thus, it is reasonable to use the Hillas model to parameterize the UHECR flux of the boosted CνB above $5 \times 10^8 \text{ GeV}$ [40].

Star formation rate (SFR) source evolution. The cosmic star formation rate density follows the empirical parameterization from [74]:

$$\rho(z) = \frac{(a + bz)h}{1 + (z/c)^d} M_\odot \text{ yr}^{-1} \text{ Mpc}^{-3}, \quad (24)$$

where $h \equiv H_0/(100 \text{ km s}^{-1} \text{ Mpc}^{-1})$ is the dimensionless Hubble parameter, with $a = 0.0170$, $b = 0.13$, $c = 3.3$, and $d = 5.3$. The normalized source density function $f(z)$ is defined as:

$$f(z) \equiv \frac{\rho(z)}{\rho(z_{\min})}, \quad (25)$$

where $\rho(z)$ represents the raw source density at redshift z , and $z_{\min} = 0$ serves as the baseline normalization redshift.

Quasi-Stellar object (QSO) source evolution. The logarithmic density evolution follows [75]:

$$\log \rho(z) = -a_0 + a_1 z - a_2 z^2 + a_3 z^3 - a_4 z^4, \quad (26)$$

$$f(z) = \frac{\exp(\log \rho(z))}{\exp(\log \rho(z_{\min}))}, \quad (27)$$

with coefficients $a_0 = 12.49$, $a_1 = 2.704$, $a_2 = 1.145$, $a_3 = 0.1796$, and $a_4 = 0.01019$.

Gamma-Ray burst (GRB) source evolution. The GRB rate is modeled by scaling the star formation rate

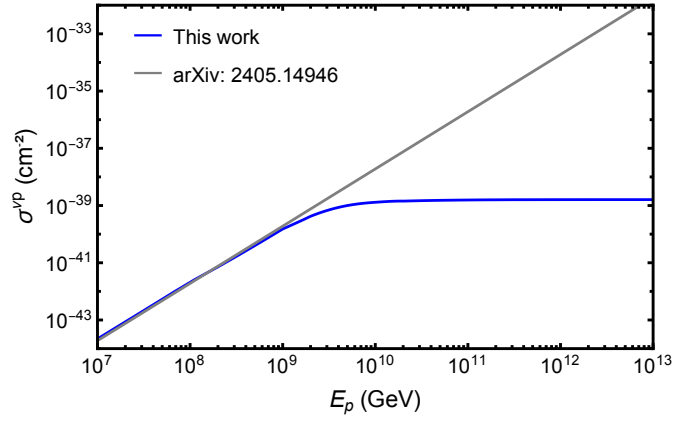


FIG. 7. The neutral current neutrino-proton cross section as a function of the proton energy. The blue line indicates the energy-dependent cross section adopted in this work, and the gray line shows the one used in Ref. [15].

(SFR) density following [76]:

$$\rho_{\text{GRB}}(z) = \kappa \rho(z)(1+z)^\delta, \quad (28)$$

where $\rho(z)$ is the SFR density defined in Eq. (24), $\kappa = 8.5$, and $\delta = 1.26$. The normalized density function $f(z)$ is then computed using Eq. (25).

Fig. 6 illustrates the boosted $C\nu B$ flux and constraints on the overdensity parameter η for different CR source distributions, including gamma-ray bursts (GRB, left panels) and quasar distribution (QSO, right panels), following the setup of Fig. 4. When m_1 is 0.1 eV, IceCube constrains $\eta < 8.1 \times 10^5$, while Pierre Auger constrains $\eta < 1.39 \times 10^7$. With a decrease in the lightest neutrino mass to $m_1 = 0.01$ eV, IceCube constrains $\eta < 1.1 \times 10^7$, and Pierre Auger constrains $\eta < 1.9 \times 10^8$. The GRB source distribution provides the strongest constraints, while those from the QSO distribution are approximately an order of magnitude weaker, and the constraints from SFR, as shown in Fig. 4, are intermediate between the two.

Section C. Comparison of the elastic neutrino-proton cross section

Here we compare the neutrino-proton elastic scattering cross section with the analysis of Ref. [15], which result in an overestimation of the boosted $C\nu B$ flux and overly stringent constraints on the overdensity parameter η . The key issue lies in their treatment of the differential scattering cross section for UHECRs interacting with the $C\nu B$. Ref. [15] use $\sigma^{\nu p}/E_\nu^{\text{max}}$ as an approximation for $d\sigma^{\nu p}/dE_\nu$ (see Eq. (1) in Ref. [15]). However, as shown in Fig. 7, the $\sigma^{\nu p}$ used Ref. [15] only agree with our results at low energies and it is several orders of magnitude larger than ours at high energies. The main reason is that the $\sigma^{\nu p}$ used in Ref. [15] has neglected the energy dependence of the nucleon form factor in $d\sigma^{\nu p}/dE_\nu$. In particular, $d\sigma^{\nu p}/dE_\nu$ approach zero at high energies. This oversimplification of cross section will lead to an inflated $C\nu B$ flux prediction. Similar issues have also been discussed in the context of boosted dark matter [77].

Section D. Impact of the lightest neutrino mass and the inverted mass ordering

In the case of the normal neutrino mass ordering, we calculate the contributions of coherent and incoherent scattering to the boosted $C\nu B$ flux for different lightest neutrino masses, as shown in Fig. 8, considering all nuclei except for protons. As the lightest neutrino mass m_1 decreases, the boosted $C\nu B$ flux decreases. However, for $m_1 < 0.01$ eV, the total flux no longer changes, as the dominant contributions arise from the heavier masses m_2 and m_3 , which are less affected by the reduction in m_1 . Furthermore, since the momentum transfer $q^2 = 2m_\nu E_\nu$ depends on the neutrino mass, a smaller m_1 reduces q^2 at a given energy E_ν , thereby extending the energy range where coherent scattering dominates to a higher energy.

To investigate the impact of the inverted neutrino mass ordering on the boosted $C\nu B$ flux, we plot Fig. 9, which adopts the same setup as Fig. 4 except for an inverted mass ordering with $\Delta m_{23}^2 = 2.486 \times 10^{-3} \text{ eV}^2$ and $\Delta m_{21}^2 =$

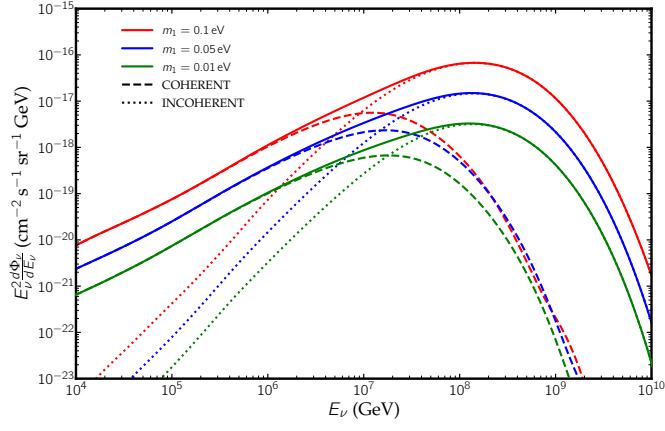


FIG. 8. The total boosted CνB flux at Earth for different lightest neutrino masses m_1 . Solid lines show the total flux from all nuclei (excluding protons) in red ($m_1 = 0.1$ eV), blue ($m_1 = 0.05$ eV), and green ($m_1 = 0.01$ eV), with dashed and dotted lines correspond to the coherent and incoherent contributions, respectively. Here we use the SFR model for CR source evolution with $\eta = 1$.

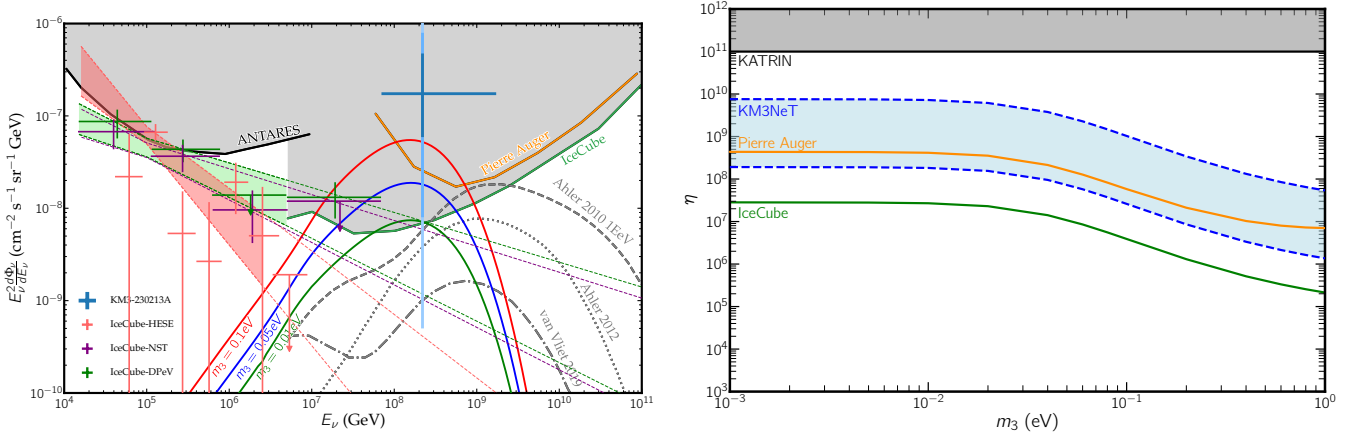


FIG. 9. Same as Fig. 4, except for the case of inverted neutrino mass ordering.

$7.42 \times 10^{-5} \text{ eV}^2$ [42]. In the left panel, the flux for $m_3 = 0.1$ eV and $m_3 = 0.05$ eV shows negligible differences compared to the normal ordering, indicating that the boosted flux remains relatively insensitive to these mass values. However, for $m_3 = 0.01$ eV, the neutrino flux increases by approximately 50% compared to the normal ordering. Similarly, in the right panel, this feature is also observed for $m_3 < 0.01$ eV.